Journal of Materials Chemistry

Dynamic Article Links

Cite this: *J. Mater. Chem.*, 2012, **22**, 23935

www.rsc.org/materials

PAPER

Charge trapping behavior in organic–inorganic alloy films grown by molecular layer deposition from trimethylaluminum, *p*-phenylenediamine and water

Wenhao Zhou, Jina Leem, Inhye Park, Yinshi Li, Zhenyu Jin and Yo-Sep Min*

Received 16th August 2012, Accepted 20th September 2012
DOI: 10.1039/c2jm35553a

Organic–inorganic hybrid or alloy films have great potential as a functional material because they have structural flexibility owing to the presence of an organic moiety. Here organic–inorganic hybrid films were grown by molecular layer deposition (MLD) by using trimethylaluminum and *p*-phenylenediamine. Although the hybrid films could be grown *via* the self-limiting growth mechanism of MLD, the hybrid films were severely air sensitive. The stability problem of the hybrid films could be solved by alloying the hybrid layer with Al_2O_3 layers. The alloy films, which were grown by repeating supercycles with one subcycle for the hybrid layer and four subcycles for the Al_2O_3 layers, showed excellent dielectric properties: a leakage current density of $\sim 2.3 \times 10^{-8}$ A cm^{-2} at 1 MV cm^{-1}; a dielectric breakdown field at $\sim$2.9 MV cm^{-1}; and a dielectric constant of $\sim$6.2. Interestingly, charge trapping behavior was clearly observed in the alloy film. The charge trapping ability of the alloy film was verified with a charge trapping memory capacitor in which the alloy film was inserted as a charge trapping layer.

Introduction

Atomic layer deposition (ALD) is one of the vapor deposition methods to grow various thin films, including oxides, nitrides, and metals, *via self-limiting chemisorption*.[1–3] In ALD an appropriate precursor vapor and a reaction gas are alternately exposed onto a substrate of which the temperature is maintained to be low enough in order to avoid thermal decomposition of the precursor. The reaction chamber is purged with an inert gas between the pulses of the precursor vapor and the reaction gas. Each cycle of the ALD process generally consists of precursor exposure–purge–reaction gas exposure–purge. The film growth occurs through chemisorption between the gaseous molecules (*i.e.*, precursor vapor or reactant gas) and reactive functional groups on the surface (*e.g.*, hydroxyl groups or chemisorbed organometallic groups). Once vacant adsorption sites become saturated by adsorbate molecules to form one monolayer (practically a sub-monolayer is formed due to the bulkiness of adsorbate molecules), the precursor or reactant gases in excess do not chemically adsorb on the monolayer. Consequently the film growth by ALD is self-limiting.

Owing to the self-limiting mechanism, ALD generally gives excellent thickness control, uniform growth over large areas and conformal films on three dimensional structures. Similar self-limiting surface reactions can be also employed for organic polymer thin films such as polyamides and polyimides by using bifunctional organic monomers.[4–10] This modification of ALD for organic polymer films is described as molecular layer deposition (MLD) because a molecular fragment of an organic precursor is deposited during each ALD cycle.

The functionalities of MLD for an organic layer and ALD for an inorganic film suggest an extended approach to organic–inorganic hybrid or alloy films. Several groups reported hybrid polymer films called metalcones (*e.g.*, alucone, zincone, titanicone and zircone) which are based on a family of reactions between a metal precursor (*e.g.*, trimethylaluminum (TMA), diethylzinc, titanium tetrachloride, and zirconium tetra-*t*-butoxide) and a diol (*e.g.*, ethylene glycol).[11–15] In addition to metalcones by MLD, various organic–inorganic hybrid materials have been investigated to form thin films because of the potential of combining distinct properties of organic and inorganic moieties in the hybrid materials.[14–18]

Organic–inorganic hybrid films can serve as scaffolds to obtain porous oxide films of the inorganic elements by calcination.[23] Functional materials such as transparent conducting films and organic magnetic films have been recently investigated by using MLD.[24,25] New applications of MLD have been proposed in various fields, *e.g.*, cancer therapy and lithographic patterning.[26,27] However, the application of organic–inorganic hybrid films is limited because they are rather air-sensitive due to the presence of labile organic moieties in the films.[11–15] Therefore, in order to improve the stability of MLD films, two methods have been tried: cross-linking the organic moieties or alloying the MLD hybrid layer with the ALD inorganic layer.[14,15,19,20,22,28]

Department of Chemical Engineering, Konkuk University, 1 Hwayang-Dong, Gwangjin-Gu, Seoul, 143-701, Korea. E-mail: ysmin@konkuk.ac.kr

George *et al.* have recently reported that alucone MLD layers and Al_2O_3 ALD layers could be mixed to obtain the alloy films with tunable density.[28] Because the alucone MLD film usually has a lower density than the Al_2O_3 ALD film, the density of the alloy films could be varied by adjusting the relative number of ALD and MLD cycles in the reaction sequence. It is a typical approach to compromise dielectric constant and leakage current in high-k thin films.[29,30]

Nowadays organic thin film transistors (OTFTs) have attracted great attention as a promising building block of flexible electronics.[31–33] It was demonstrated that organic–inorganic hybrid or alloy films by MLD could be employed as gate-dielectrics or semiconducting films in the OTFTs.[17,19,34,35] Even though the use of the organic–inorganic hybrid or alloy films has been extended to various applications, there is not any report yet in which the organic–inorganic hybrid or alloy films are utilized as a memory component in electronic memory devices.

In this work, organic–inorganic hybrid films by MLD from TMA and *p*-phenylenediamine (PPD, $C_6H_4(NH_2)_2$) are alloyed with Al_2O_3 ALD layers in order to improve the stability of the hybrid film. The electrical and dielectric properties were characterized for the alloy films. Furthermore, we report a clear observation of charge trapping behavior in the alloy films. The charge trapping ability of the alloy film was verified with a charge trapping memory capacitor for nonvolatile charge trap flash memories.

Experimental

All thin films were grown on boron doped p-type (100) Si wafers, of which resistivity is 5–20 Ω cm, by using a laminar flow type ALD reactor (ATOMIC-CLASSIC 2nd edition, CN-1 Co., Ltd.). Although our reactor could process a 6 in. wafer, five square specimens (2×2 cm^2) were loaded on the center, left, right, top and bottom positions of the 6 in. substrate holder in order to evaluate non-uniformity in the 6 in. wafer. The specimens were used without removing the native oxide. TMA (UP Chemical Co., Ltd) and water were vaporized from external canisters at room temperature and led into the reactor through solenoid valves without any carrier gas. The doses of TMA and water were $\sim 1.0 \times 10^{-4}$ and $\sim 7.2 \times 10^{-5}$ mol s^{-1}, respectively. PPD (Sigma-Aldrich) was vaporized at 145 °C with a high purity (99.999%) N_2 gas (100 standard cubic centimeters per minute, sccm) and carried into the reactor with a dose of $\sim 2.8 \times 10^{-6}$ mol s^{-1}. For purging the reactor, the high purity N_2 gas was used with a flow rate of 400 sccm. All delivery lines were maintained at 120 °C. The specimen temperatures, which were calibrated with a thermocouple-implanted 6 in. wafer, were determined in the temperature range of 200–400 °C. The base pressure of the reactor was less than 10 mTorr and ALD was processed at a working pressure range of 200–600 mTorr.

Fig. 1 shows a schematic diagram of our MLD process flow for the growth of organic–inorganic alloy films from TMA, PPD and water. X and Y are the numbers of subcycles for hybrid layers and Al_2O_3 layers, respectively. N is the number of supercycles for the alloy films. The MLD hybrid layers were grown by alternately exposing TMA (1 s) and PPD (7 s except for Fig. 3 and 7), and the purge times for TMA and PPD in this MLD sequence were 30 and 60 s, respectively. The ALD Al_2O_3 layers were

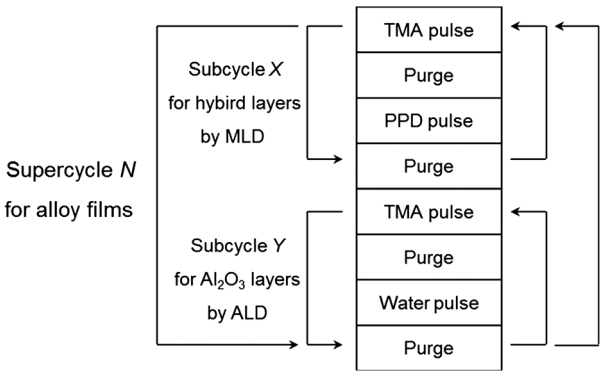

Fig. 1 Schematic diagram of the MLD process for organic–inorganic alloy films from TMA, PPD and water.

deposited from TMA and water as an Al precursor and a reactant gas, respectively. After the TMA and water pulses for 1 s, the reactor was purged for 10 s. Several alloy films (1 : 1, 1 : 2, 1 : 3, and 1 : 4) were grown by adjusting the values of X and Y, and the thicknesses of them were controlled by N. The X : Y alloy film designates an organic–inorganic alloy film grown by repeating N supercycles in which X and Y subcycles are iterated for the hybrid layer and the Al_2O_3 layer, respectively.

All thicknesses of the grown films were measured by a spectroscopic ellipsometer (SE, MG-1000, NanoView). The incident angle of the polarized light in the SE was fixed at around 70°, and the incident light has a spectral range of 1.5–5.0 eV. In order to determine an initial value of the thickness for fitting the measured data, they were firstly fitted with Al_2O_3 reference values of the real and imaginary parts of the complex dielectric function supplied by NanoView.[36] Subsequently the measured data were fitted with the Cauchy dispersion function for all films.[37]

By using five thicknesses obtained at the center, top, bottom, left and right positions in the 6 in. substrate holder, non-uniformity of the MLD process was evaluated by dividing the standard deviation of the thicknesses by the mean values. The stability of the films was estimated by measuring the change in thickness of films which were exposed to atmosphere at room temperature.

X-ray photoelectron spectroscopy (XPS) spectra were collected on an AXIS-NOVA (Kratos Inc.) spectrometer using Al Kα emission (1486.6 eV). Binding energies were measured using the C 1s peak (285.0 eV) of the adventitious carbon as an internal standard. A high resolution transmission electron microscopic (HR-TEM) image was obtained on a cross-section of the memory capacitor which was prepared by focused ion beam of gallium ion.

In order to examine the electrical properties of the alloy films, capacitors with a structure of Au/alloy film/native SiO_2 (2 nm)/p-Si(100) were fabricated by depositing 50 nm thick Au films by thermal evaporation through a metal shadow mask for the top electrodes. The area of the Au electrode was $\sim 1.26 \times 10^{-3}$ cm^2. Flash memory capacitors were also prepared with a 1 : 4 alloy film as a CTL. The structure of the memory capacitor was Au (50 nm)/Al_2O_3 (20.5 nm)/alloy film (1.4 nm)/Al_2O_3 (6.5 nm)/SiO_2 (2 nm)/p-Si in which the thick and thin Al_2O_3 films played the roles of a blocking oxide and a tunnel oxide, respectively. The tunnel Al_2O_3 (ALD 70 cycles), the CTL (1 : 4 alloy, $N = 3$) and

the blocking Al_2O_3 (ALD 220 cycles) were continuously deposited at 400 °C on a p-Si substrate with native SiO_2 without breaking vacuum of the reactor. Current density–voltage (J–V) and capacitance–voltage (C–V) characteristics of the capacitors were measured with a semiconductor parameter analyzer (HP 4145B) and a LCR meter (HP 4284A), respectively.

Results and discussion

Organic–inorganic hybrid films from TMA and PPD

The surface reactions for MLD of organic–inorganic hybrid films ($X = N$ and $Y = 0$) are proposed as shown in Fig. 2. In the first half-reaction of MLD, amino groups (or hydroxyl groups for the first cycle) on the surface are exposed to TMA, and methane is released as a byproduct. The resulting surface is exposed to PPD in the second half-reaction and methane is again released as a byproduct. Consequently, the amino groups on the surface are recovered for the next cycle.

Fig. 3 shows thickness variation of the organic–inorganic hybrid films as a function of the exposure time of PPD. The hybrid films were deposited at 400 °C by MLD ($X = N = 50$ and $Y = 0$). As the exposure time of PPD increases, the thickness initially increases and then saturates above 5 s. Although the self-limiting growth of the hybrid films is observed in the MLD, the thicknesses were not uniform in the 6 in. wafer scale, and the thickness uniformity is not reproducible in run-to-run investigation mainly due to the poor stability of the film in air.

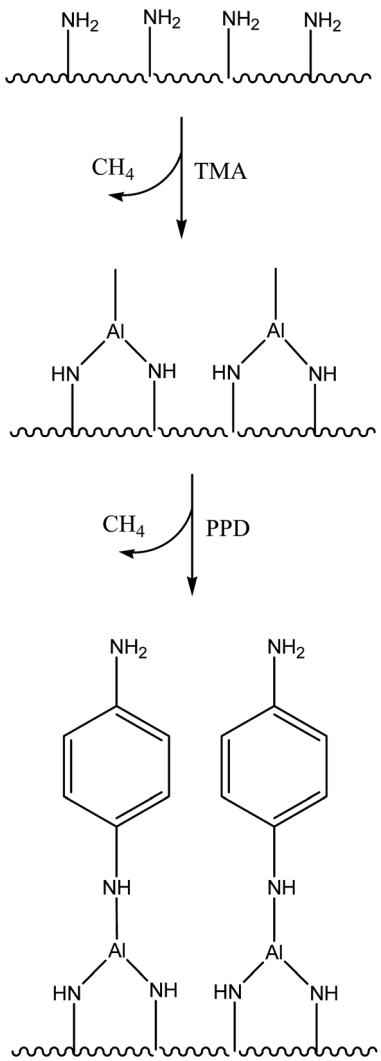

Fig. 2 Schematic diagram of MLD reaction sequence for the organic–inorganic hybrid film growth using TMA and PPD.

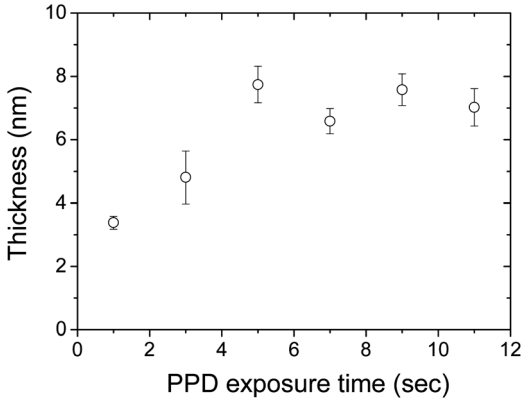

Fig. 3 Thickness of the hybrid films ($X = N = 50$ and $Y = 0$) grown at 400 °C as a function of the PPD exposure time.

Generally metalcones show a decrease in thickness when exposed in air after MLD. However our hybrid films show a severe increase in thickness; for example, after 2 weeks the thickness was increased by ~30% as shown in Fig. 4.[11–15] Sood *et al.* reported MLD of Ti–4,4′-oxydianiline hybrid films which were stable in atmospheric air when they were grown in the range of 250–490 °C while the films grown at lower temperatures (160–230 °C) showed instability in air.[21] Even though the chemical mechanism of the increase in thickness is not clear, we predict it may be due to undesirable chemical reactions between the hybrid film and moisture (and/or oxygen). The undesirable reaction may occur from the surface of the hybrid film leaving a chemically changed layer. This phenomenon is similar to the silicon oxide growth from the Si substrate under the exposure of O_2 or H_2O.

Deal and Grove's model describes the kinetics of silicon oxidation.[38] According to their model, in an initial stage of the

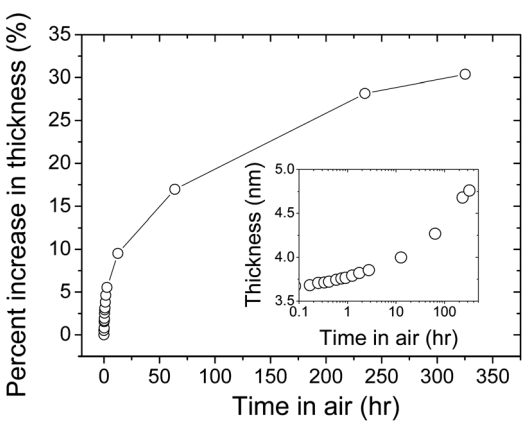

Fig. 4 Percent increase in the thickness of a hybrid film ($X = N = 50$ and $Y = 0$) grown at 400 °C as a function of exposure time in air. The inset shows the thickness variation as a function of time in logarithmic scale.

oxide growth from Si, the thickness of the oxide is linear with the oxidation time because of the reaction-controlled oxidation. However for a long oxidation time, the oxide thickness is proportional to the square root of the oxidation time, since the oxidation is diffusion-controlled due to the presence of the oxide layer between O_2 (or H_2O) and Si. Similarly, the increase in the thickness of the hybrid film is initially linear with the exposure time in air, and then it shows parabolic kinetics because the chemical change of the hybrid film may be rather diffusion-controlled owing to the presence of the chemically changed layer between air and the unchanged hybrid layer.

Fig. 5 shows XPS spectra (the upper) of the hybrid film ($X = N = 50$ and $Y = 0$) grown at 400 °C which was exposed in air for several months. The lowest binding energy C 1s peak assumed to be from adventitious C–H species was set to 285.0 eV to calibrate the other peaks.[11] The clear peak of carbon located at higher binding energy (~288.9 eV) is generally associated with highly electron withdrawing C=O group.[11,39–41] According to the proposed reaction scheme in Fig. 2, there should be no C=O species in the hybrid film. Although it can also be from adventitious carbon, we speculate that the peak is originated from the chemical change in the hybrid film by H_2O and/or O_2 when exposed in air. Indeed the O 1s peak, which should be absent in the hybrid film, is also observed at ~531.6 eV.

The Al 2p peak appears at ~74.5 eV, as predicted in Fig. 2, the N 1s peak is observed at ~399.5 eV which is slightly smaller than the reported value (~399.8 eV) of PPD.[41] It has been recently reported that the binding energy ranges of N^+, N^{2+} and N^{3+} oxidation states in aluminum oxynitride are 399.3–399.9 eV, 402.0–402.3 eV and 404.1–404.5 eV, respectively.[42,43] The position of N 1s peak in Fig. 5 is similar to the N^+ oxidation state, presumably due to the chemical change in the hybrid film in air.

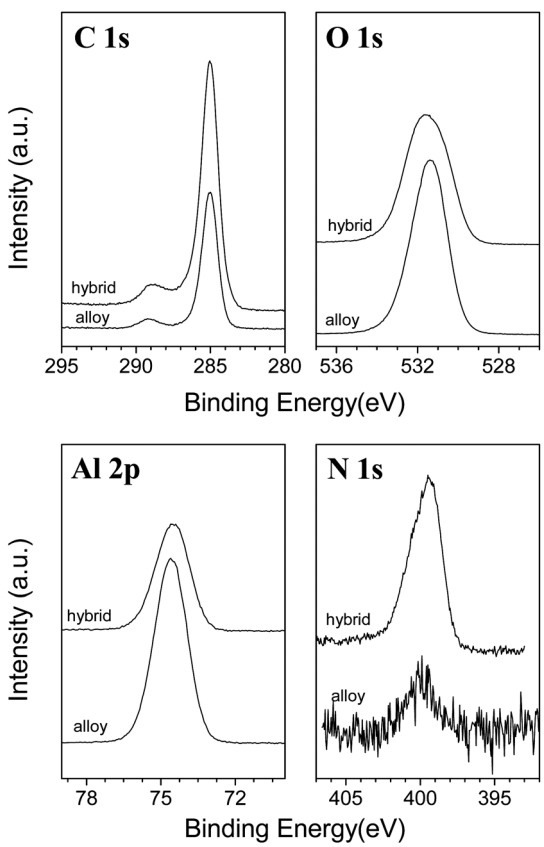

Fig. 5 X-ray photoelectron spectra of the hybrid ($X = N = 50$ and $Y = 0$) and the 1 : 4 alloy thin films grown at 400 °C.

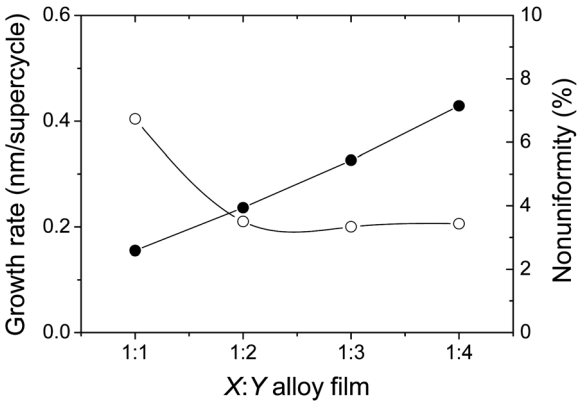

Fig. 6 Thickness (solid circles) and non-uniformity (open circles) of the X : Y alloy films grown at 400 °C.

Organic–inorganic alloy thin films

Because of the poor stability of the hybrid films in air, the hybrid layer was alloyed with Al_2O_3 layers. Fig. 6 shows the growth rate (the grown thickness per supercycle) of the X : Y alloy films grown at 400 °C. The number of subcycles for the hybrid layer was fixed at $X = 1$. As the subcycle (Y) for the Al_2O_3 layer increases by 1, the growth rate becomes faster linearly. The increase (0.092 nm per supercycle) in the growth rate, when increasing Y by 1, is well-agreed with the typical growth rate of Al_2O_3 films at 400 °C by TMA and water. Furthermore the non-uniformity of the alloy films in 6 in. wafer-scale is also highly improved as Y increases since the labile hybrid layer may be protected from the air exposure by the Al_2O_3 layer. Indeed the 1 : 4 alloy film showed a much smaller increase in thickness, less than 5%, after several tens of weeks while the thickness of the hybrid film increased by 30% in 2 weeks under air exposure.

The 1 : 4 alloy films grown at 400 °C show clear self-limiting growth behavior at longer exposure times than 7 s (Fig. 7). In

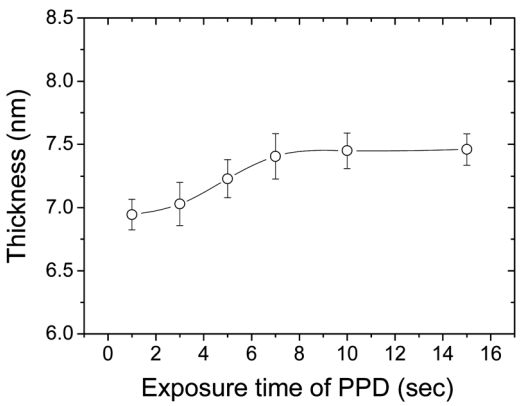

Fig. 7 Thickness of the 1 : 4 alloy films ($N = 20$) grown at 400 °C as a function of the PPD exposure time.

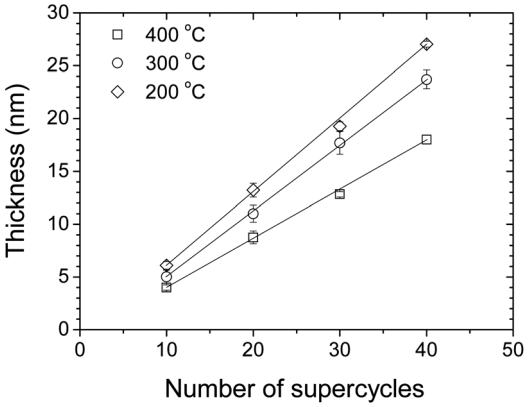

Fig. 8 Thickness of the 1 : 4 alloy films *versus* number of supercycles for a variety of growth temperatures (diamonds 200 °C; circles 300 °C; squares 400 °C). The error bars denote the standard deviations of the thicknesses.

comparison to Fig. 3, the thickness of the alloy films slowly saturates, presumably due to higher density of adsorption sites on the Al_2O_3 layer than on the hybrid layer.

To investigate the linear growth of the 1 : 4 alloy films with respect to the number of supercycles, the alloy films were grown at a temperature range of 200–400 °C for 10, 20, 30 and 40 supercycles, respectively. Among them, the thickness data at 200, 300 and 400 °C are shown in Fig. 8 (data at 250 and 350 °C not shown for clarity). The thickness of the alloy films linearly increases with the number of supercycles as typically expected in ALD and MLD. The growth rates of the alloy films, determined from the slopes in Fig. 8, at each growth temperature are plotted as squares in Fig. 9. Although the growth rate of the 1 : 4 alloy films becomes smaller at higher temperatures (0.69 nm per supercycle at 200 °C to 0.46 nm per supercycle at 400 °C), the typical plateau in the growth temperatures due to the self-limiting chemisorption is observed in a range of 350–400 °C.

Because of the poor stability of the hybrid films, it was practically difficult to determine the growth rate of the hybrid film. Therefore we performed ALD of Al_2O_3 films at the same temperature range with the alloy films as shown with circles in Fig. 9. Using the growth rates of Al_2O_3 films at each growth

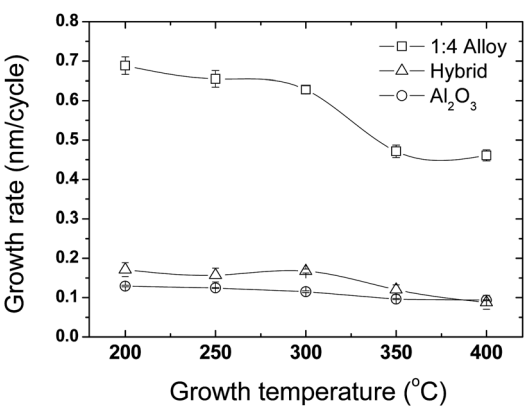

Fig. 9 Growth rates of the 1 : 4 alloy films (squares), the hybrid films (triangles) and Al_2O_3 films (circles) as a function of growth temperature. The error bars denote the standard deviations of the growth rates.

temperature, the growth rate of the hybrid layer in the alloy film can be indirectly evaluated as shown with triangles in Fig. 9. As a result, the growth rate of the hybrid layer is in the range of 0.09–0.17 nm per subcycle. Furthermore, the non-uniformities (in 6 in. wafer-scale) of the hybrid layer (~2.0%) and the 1 : 4 alloy film (~3.1%) at 400 °C was good enough to be compared to that of the Al_2O_3 film (~1.1%) at the same temperatures. Thus the 400 °C was determined to be the growth temperature for device fabrication.

Fig. 5 also shows XPS spectra of the 1 : 4 alloy film (the lower) grown at 400 °C. Because the hybrid layer ($X = 1$) was alloyed and atomically mixed with the Al_2O_3 layer ($Y = 4$), the intensities of C 1s and N 1s peaks are significantly reduced in comparison to those of the hybrid film. Since nitrogen atoms are severely less sensitive in XPS, the N 1s peak in the 1 : 4 alloy film is much weaker. In contrast, the Al 2p and O 1s peaks are much stronger due to the presence of the Al_2O_3 layers.

Electrical properties of the alloy films

Electrical properties of the 1 : 4 alloy films grown at 400 °C for 100 supercycles were characterized on a capacitor structure (Au/alloy (46 nm)/SiO_2 (2 nm)/p-Si). The capacitor area was 1.26×10^{-3} cm^2, defined by using a shadow mask during Au deposition. Fig. 10a shows a current density–electrical field (J–E) curve of the 1 : 4 alloy film. The leakage current density is $\sim 2.3 \times 10^{-8}$ A cm^{-2} at an electric field of 1 MV cm^{-1}, which is slightly higher than the reported values (10^{-8} to 10^{-9} A cm^{-2}) of the Al_2O_3 films grown from TMA.[44,45] However the dielectric breakdown of the alloy film appeared at ~2.9 MV cm^{-1}, which is much lower than the breakdown field (6–8 MV cm^{-1}) of Al_2O_3 films, possibly due to the presence of the organic moieties in the alloy films.[45,46]

Fig. 10b shows a capacitance–voltage (C–V) curve of the Au/alloy/SiO_2/p-Si at 100 kHz. It shows the typical features of an n-type metal–oxide–semiconductor (n-MOS) capacitor with an accumulation region at negative applied voltages and an inversion region at positive voltages.[47,48] The variation of capacitance with the applied voltage is caused by changes in the thickness of the carrier depletion region (*i.e.*, space charge region) of the p-Si substrate. At large negative voltages where the silicon surface is in accumulation, the measured capacitance is approximately equal to the serial capacitance of the 1 : 4 alloy and the native SiO_2 layers. Considering the 2 nm thick native oxide of which the dielectric constant is ~3.9, the estimated dielectric constant of the 1 : 4 alloy films is ~6.2 from the serial capacitance equation:

$$1/C_D = 1/C_{SO} + 1/C_A \quad (1)$$

where C_D is the dielectric capacitance measured at the accumulation region (−4 V), and C_{SO} and C_A are the capacitance from SiO_2 and the alloy, respectively. The value of the dielectric constant is significantly lower than the dielectric constant (7–8) of ALD Al_2O_3 films,[45,46] since the 1 : 4 alloy film contains an organic moiety.

Considering the resistivity (5–20 Ω cm) of p-Si used, the doping concentration of p-Si is $\sim 1 \times 10^{15}$ cm^{-3}.[47] The work function (ϕ_M) of Au is 5.31–5.47 eV depending on its crystalline plane,[49] and the electron affinity (χ) of Si is 4.05 eV.[47] The work function difference (ϕ_{MS}) between Au and p-Si is determined by the equation:

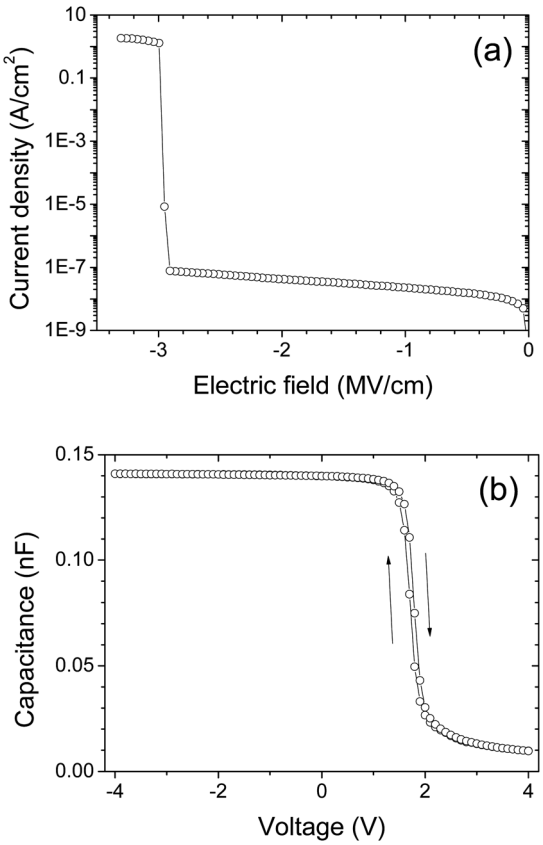

Fig. 10 Current density–electric field curve (a) and capacitance–voltage curve (b) measured from an Au/1 : 4 alloy (46 nm)/SiO_2 (2 nm)/p-Si capacitor. The 1 : 4 alloy film was grown at 400 °C for 100 supercycles. The absolute values of current density were taken to plot the curve in logarithmic scale.

$$\phi_{MS} = \phi_M - (\chi + (E_C - E_F)/q) \quad (2)$$

where q, E_C and E_F are the magnitude of electron charge, conduction band edge and Fermi energy, respectively.[48] Using the doping concentration and the intrinsic carrier concentration ($\sim 1 \times 10^{10}$ cm^{-3}) of Si at room temperature,[47] the value of $E_C - E_F$ is ~0.86 eV, and consequently ϕ_{MS} is evaluated to be around 0.40–0.56 eV.

If the as-grown alloy film, native oxide, and the interfaces are free of charges, the flat band voltage (V_{FB}) is equal to ϕ_{MS}/q between Au and Si.

$$V_{FB}\ (\text{free of charges}) = \phi_{MS}/q \quad (3)$$

However, as shown in Fig. 10b, V_{FB} was determined to be around 1.8 V from the flat band capacitance (C_{FB}) of ~0.06 nF, which was calculated from the equation:

$$C_{FB} = 1/(1/C_D + L_D/A\varepsilon_s)\ \text{at}\ V_{FB} \quad (4)$$

where A is the area of the capacitor (1.26×10^{-3} cm^2), L_D is the Debye length (0.13 μm at the doping concentration of 1×10^{15} cm^{-3}) and ε_s is the permittivity ($11.9 \times 8.854 \times 10^{-14}$ F cm^{-1}) of silicon.[50] Comparing the values of V_{FB} (1.8 V) and ϕ_{MS}/q (0.40–0.56 V), we observed a positive flat band voltage shift (ΔV_{FB} = 1.24–1.40 V). Generally the V_{FB} is shifted from ϕ_{MS}/q under the presence of charge density (Q) by the equation:[47]

$$V_{FB} = \phi_{MS}/q - QA/C_D \quad (5)$$

and subtracting eqn (3) from eqn (5),

$$\Delta V_{FB} = -QA/C_D \quad (6)$$

Therefore the positive shift ($\Delta V_{FB} > 0$) is attributed to negative charges in the capacitor dielectric. Since the number density (N) of charges can be simply calculated by $N = Q/q$, N can be expressed by substituting $Q = qN$ to eqn (6):

$$N = \Delta V_{FB} C_D/qA \quad (7)$$

Thus, the number density of the negative charges in the capacitor is in the range of 8.7×10^{11} to 9.8×10^{11} cm^{-2}.

Among various charges such as fixed charges, oxide-trapped charges and interface-trapped charges, the parallel shift of the C–V curve is generally attributed to fixed charges.[47,48,50] Since the fixed charges in the SiO_2/Si structure are usually low (a few 10^{10} cm^{-2}) enough to be negligible compared to the estimated value, it is believed that the negative fixed charges are mainly contributed from the alloy film and/or the interface with SiO_2.

One more concern for the C–V curve is a clockwise hysteresis, as denoted with arrows in Fig. 10b, when the applied voltage is reversely swept from the inversion to the accumulation (from 4 V to −4 V) and then forwardly swept back to the inversion (from −4 V to 4 V). Generally hysteresis is attributed to charges trapped in the bulk of the dielectric.[48] Recently, Jeong and Lee have reported that an organic–inorganic hybrid film (amino-propyl-silsesquioxane) shows a distinct clockwise hysteresis and the nitrogen-related molecular defects act as electron trap centers.[51] Yoshida *et al.* also reported the charge trapping effect of a MLD polyimide film.[52] It is believed that the hysteresis originates from the charge trap centers in the alloy film where electrons or holes can be trapped depending on the polarity of the applied voltage. When the positive voltage is applied in the reverse sweep, holes may be injected from the top electrode to the traps of the alloy, and the positively charged trap sites results in the negative flat band shift (*i.e.* the negative shift of the C–V curve) according to eqn (6). Similarly, the negatively charged trap sites formed by the electron injection in the forward sweep give rise to the positive flat band shift (*i.e.* the positive shift of the C–V curve). It should be noted that the charge injection from the substrate may not be preferred to that from the top electrode due to the presence of native SiO_2 between the alloy film and Si.

Charge trapping behavior of the alloy films

In order to verify the charge trapping ability of the alloy film, we fabricated a flash memory capacitor structure which is comprised of a top electrode, blocking oxide, charge trap layer (CTL), tunnel oxide and p-Si substrate.[53] The HR-TEM image in Fig. 11a shows a cross-sectional view of the memory stack. Although the native SiO_2 and Si substrate are clearly seen, it is difficult to differentiate between the tunnel Al_2O_3, CTL (1 : 4 alloy) and the blocking Al_2O_3. It should be noted that the three layers in the memory stack are intrinsically based on Al_2O_3.

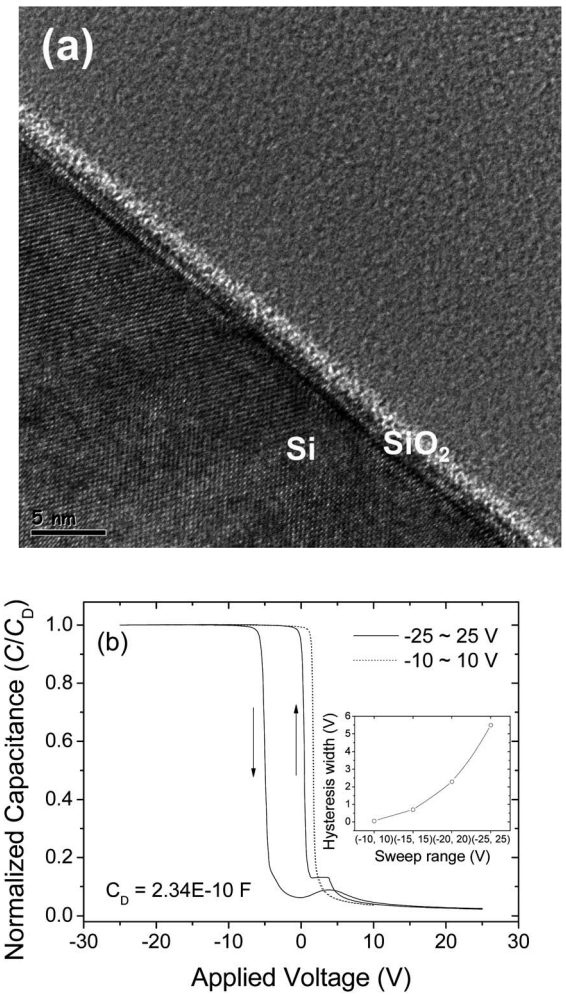

Fig. 11 (a) Cross-sectional image of HRTEM in the memory capacitor. (b) Normalized capacitance *versus* applied voltage curves in the sweep ranges of −10 to 10 V (dotted line) and −25 to 25 V (solid line). The inset shows the width of hysteresis *versus* the sweep range.

Additionally this picture supports the fact that the 1 : 4 alloy was formed by atomically mixing the hybrid layer and the Al_2O_3 layer.

In the operation of the charge trap flash memory, by applying a positive voltage pulse on the top electrode, electrons are trapped in the CTL (or holes are ejected from the CTL) through the tunnel oxide from Si, which is called 'programming'. 'Erasing' is achieved by applying a negative voltage pulse on the top electrode. Under the erasing voltage, electrons escape from the trap sites (or holes are trapped) in the CTL to the Si substrate. Therefore it is required that the CTL should show a large hysteresis in its *C–V* curve like the typical CTL, the Si_xN_y film, because the width of the hysteresis is utilized as a memory window for programming and erasing.[53] In addition, the tunnel oxide should be thin enough to allow the tunnelling of charge carriers, and the blocking oxide should be thick in order to prevent charge injection from the top electrode.

Recently new CTL materials such as nanodots, graphene and organic–inorganic hybrid films have been investigated to replace the Si_xN_y film for the emerging application of charge trap flash memory.[54–56] Here we use the 1 : 4 alloy film as a CTL. In our memory capacitor, except for the Au electrode, all layers of blocking oxide (Al_2O_3, 20.5 nm), CTL (the 1 : 4 alloy film, 1.4 nm) and tunnel oxide (Al_2O_3, 6.5 nm) were continuously grown on SiO_2 (2 nm)/p-Si without breaking vacuum of the ALD reactor, which is an important advantage of our memory structure in terms of fabrication.

Fig. 11b shows *C–V* hysteresis characteristics of the memory capacitor where the capacitance was normalized with the dielectric capacitance ($C_D = 2.34 \times 10^{-10}$ F) obtained at the accumulation region. The width of the hysteresis, which is approximately ΔV_{FB}, is 60 mV in a narrow sweep range (−10 to 10 V, dotted line). When reading the stored charge, the amount of the stored charge should not be varied by applying a reading voltage. Therefore it is desirable for our capacitor to show a small width of the hysteresis in the voltage range from −10 V to 10 V, since we can choose a reading voltage in the voltage range. However the width of the hysteresis increases as the sweep range increases, as shown in the inset of Fig. 11b. The hysteresis width (*i.e.*, ΔV_{FB}) dramatically increases to ~5.5 V in the wide sweep range from −25 V to 25 V. However, it should be noted that the *C–V* hysteresis in the wide sweep range was not positively shifted even after the voltage stress of +25 V compared with the *C–V* curve obtained in the narrow sweep. This suggests that electron trapping in the CTL does not occur even by such a highly positive bias due to the absence of electrons, which are the minority carrier in the p-type Si substrate. The formation of carrier inversion usually requires the presence of heavily doped n-type source and drain or high defect density in Si. However this is not the case with our memory capacitor. Thus the responsible charge carriers are holes in our memory capacitor, and the 'programming' just corresponds to the ejection of holes trapped during the previous 'erasing' voltage.

In addition, the clear counterclockwise hysteresis reveals that holes are trapped in the CTL under the applied erasing voltage (*e.g.*, −25 V), and they are ejected from the CTL under the applied programming voltage (*e.g.*, 25 V). The number density of holes trapped during sweeping of the voltage in the narrow range (−10 to 10 V) is calculated to be $\sim 7.0 \times 10^{10}$ cm^{-2} by eqn (7). However the density of holes which contribute the large width ($\Delta V_{FB} \sim 5.5$ V) of the hysteresis in the wide sweep range (−25 to 25 V) is $\sim 6.4 \times 10^{12}$ cm^{-2}. This reveals that the amounts of the trapped charges strongly depend on the applied electric field because holes should be injected from Si to the CTL by tunneling.

The programming/erasing behavior by the charge trapping in the alloy film is shown in Fig. 12. As a reference state for the erasing, we chose a state in which holes are trapped by applying −20 V for 1 s. After erasing the memory capacitor into the reference state, the programming was performed by applying 20 V for each duration time. Flat band voltages were obtained from *C–V* curves measured in a range of $V_{FB} \pm 1$ V. Similarly the V_{FB} in the erasing process (open circles) for each duration time was determined by using another reference state achieved by applying 20 V for 1 s. In Fig. 12, as the duration time becomes longer, the V_{FB} shifts positively in the programming and negatively in the erasing. This reveals that the charge density trapped in the CTL or ejected from the CTL depends on the voltage duration time according to eqn (6) where the Q is a function of the duration time.

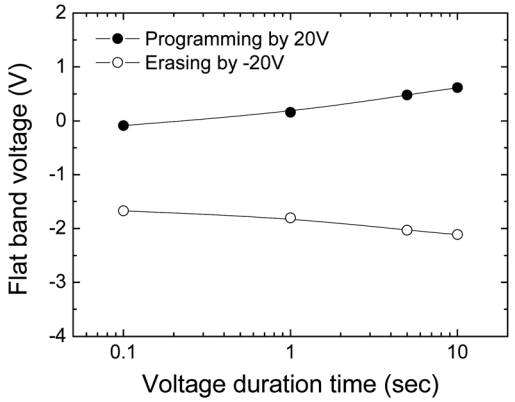

Fig. 12 Programming (solid circles) and erasing (open circles) characteristics of the memory capacitor with the 1 : 4 alloy film as a CTL. Programming and erasing voltages were 20 and −20 V, respectively.

In Fig. 13, we investigated how long the programmed charge state (solid circles) of the CTL could be retained. When the erasing voltage of −20 V was applied for 10 s (*i.e.* holes are trapped), the initial V_{FB} was −1.82 V. Subsequently, the programming was performed on the memory capacitor by applying 20 V for 10 s (*i.e.*, holes are ejected), and then we observed the variation of V_{FB} at room temperature with respect to the elapsed time as shown in Fig. 13. As the elapsed time becomes longer, the V_{FB} gradually decreases from the initial value of 0.62 V, which is attributed to re-trapping of holes. The initial density of holes ejected from the CTL is calculated to be $\sim 2.83 \times 10^{12}$ cm^{-2} using the initial value of $\Delta V_{FB} = 2.44$ V. After 10 years, the expected value of V_{FB} may be −0.62 V according to the extrapolation as shown with a dotted line in Fig. 13. Using eqn (7), the re-trapped holes for 10 years is expected to be $\sim 1.44 \times 10^{12}$ cm^{-2}. Therefore it is expected that half of the ejected holes will be re-trapped for 10 years.

Similarly, the retention characteristics of the erased state are also shown in Fig. 13 (open circles). During repeated electrical measurements, the memory capacitor used for the retention test had been electrically broken down. Thus the retention of the erased state was investigated on another capacitor in the same specimen. When programming voltage (20 V) was applied for 10 s (*i.e.*, holes are ejected), the initial V_{FB} was −0.78 V. Subsequently, the erasing voltage (−20 V) was applied for 10 s (*i.e.*, holes are trapped). After erasing, the first V_{FB} value was −2.20 V, and the extrapolated value was −1.28 V after 10 years. Therefore the initial density of holes trapped in the CTL is $\sim 1.65 \times 10^{12}$ cm^{-2} using $\Delta V_{FB} = 1.42$ V. Since ΔV_{FB} may become 0.5 V after 10 years, the retained holes in the CTL will be $\sim 5.80 \times 10^{11}$ cm^{-2}. Among the trapped, ~65% of holes will escape from the CTL for 10 years.

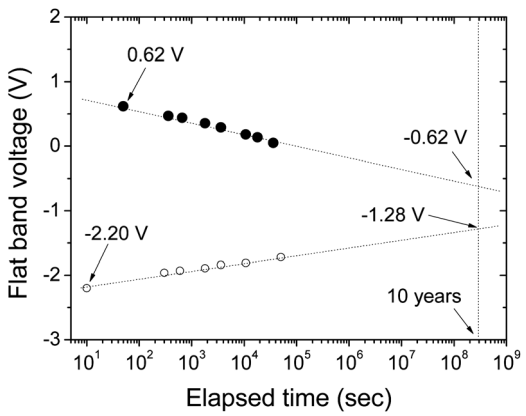

Fig. 13 Retention characteristics of the programmed (solid circles) and erased (open circles) states in the memory capacitor.

Conclusions

MLD of organic–inorganic hybrid thin films was performed by using trimethylaluminum and *p*-phenylenediamine. Although the hybrid films could be grown through the self-limiting growth mechanism, they showed severely poor stability in air. The poor stability was dramatically improved by alloying the hybrid layer with Al_2O_3 layers to form the alloy films. The alloy films showed excellent insulating properties. The leakage current density of the 1 : 4 alloy film was $\sim 2.3 \times 10^{-8}$ A cm^{-2} at an electric field of 1 MV cm^{-1}, and the dielectric breakdown field appeared at ~2.9 MV cm^{-1}. The dielectric constant of the 1 : 4 alloy film was ~6.2. Interestingly the alloy film showed clear charge trapping behavior. The possibility of the alloy film as a CTL was investigated. In terms of performance of the charge trap capacitor, the charge trapping characteristics of the alloy film are not enough to be used as a CTL for the charge trap flash memory. However here we clearly observed that charges could be trapped in our organic–inorganic alloy films. Considering the flexibility in design of the alloy films by modifying the structure of organic moieties, the CTL based on the organic–inorganic alloy films can be one of the promising candidates for the application of the emerging charge trap memory.

Acknowledgements

This research was supported by the Pioneer Research Center Program through the National Research Foundation of Korea (NRF) funded by the Ministry of Education, Science and Technology (MEST, 2011-0002125). This work was also supported by Basic Science Research Program through the NRF funded by the MEST (2011-0010556 and 2011-0013803). The authors thank Dr H. S. Baik and Mr H. J. Yun in Korea Basic Science Institute for the HR-TEM image and XPS spectra, respectively.

Notes and references

1 S. M. George, *Chem. Rev.*, 2010, **110**, 111.
2 T. Suntola, J. Antson, A. Pakkala and S. Lindfors, *SID 80 Dig.*, 1980, **11**, 108.
3 T. Suntola and J. Hyvarinen, *Annu. Rev. Mater. Sci.*, 1985, **15**, 177.
4 S. M. George, B. Yoon and A. A. Dameron, *Acc. Chem. Res.*, 2009, **42**, 498.
5 T. Yoshimura, S. Tatsuura and W. Sotoyama, *Appl. Phys. Lett.*, 1991, **59**, 482.
6 T. Bitzer and N. V. Richardson, *Appl. Phys. Lett.*, 1997, **71**, 662.
7 A. Kim, M. A. Filler, S. Km and S. F. Bent, *J. Am. Chem. Soc.*, 2005, **127**, 6123.
8 Y. Du and S. M. George, *J. Phys. Chem. C*, 2007, **111**, 8509.
9 M. Putkonen, J. Harjuoja, T. Sajavaara and L. Niinisto, *J. Mater. Chem.*, 2007, **17**, 664.
10 N. M. Adamczyk, A. A. Dameron and S. M. George, *Langmuir*, 2008, **24**, 2081.

11 A. A. Dameron, D. Seghete, B. B. Burton, S. D. Davidson, A. S. Cavanagh, J. A. Bertrand and S. M. George, *Chem. Mater.*, 2008, **20**, 3315.
12 Q. Peng, B. Gong, R. M. VanGundy and G. N. Parsons, *Chem. Mater.*, 2009, **21**, 820.
13 B. Yoon, J. L. O'Patchen, D. Seghete, A. S. Cavanagh and S. M. George, *Chem. Vap. Deposition*, 2009, **15**, 112.
14 S. M. George, B. H. Lee, B. Yoon, A. I. Abdulagatov and R. A. Hall, *J. Nanosci. Nanotechnol.*, 2011, **11**, 7948.
15 R. A. Hall, A. I. Abdulagatov and S. M. George, in *AVS 58th Annual International Symposium and Exhibition*, AVS, Nashville, Tennessee, Chico CA, October 30–November 4, 2011.
16 D. B. Mitzi, *Chem. Mater.*, 2001, **13**, 3283.
17 B. H. Lee, M. K. Ryu, S. Y. Choi, K. H. Lee, S. Im and M. M. Sung, *J. Am. Chem. Soc.*, 2007, **129**, 16034.
18 B. Yoon, D. Seghete, A. S. Cavanagh and S. M. George, *Chem. Mater.*, 2009, **21**, 5365.
19 B. H. Lee, K. K. Im, K. H. Lee, S. Im and M. M. Sung, *Thin Solid Films*, 2009, **517**, 4056.
20 P. W. Loscutoff, H. Zhou, S. B. Clendenning and S. F. Bent, *ACS Nano*, 2010, **4**, 331.
21 A. Sood, P. Sundberg, J. Malm and M. Karppinen, *Appl. Surf. Sci.*, 2011, **257**, 6435.
22 Y. Lee, B. Yoon, A. S. Cavanagh and S. M. George, *Langmuir*, 2011, **27**, 15155.
23 X. Liang, M. Yu, J. Li, Y. B. Jiang and A. W. Weimer, *Chem. Commun.*, 2009, 7140.
24 B. Yoon, Y. Lee, A. Derk, C. B. Musgrave and S. M. George, *ECS Trans.*, 2011, **33**, 191.
25 C. Y. Kao, J. W. Yoo, Y. Min and A. J. Epstein, *ACS Appl. Mater. Interfaces*, 2012, **4**, 137.
26 T. Yoshimura, C. Yoshino, K. Sasaki, T. Sato and M. Seki, *IEEE J. Sel. Top. Quantum Electron.*, 2011, **18**, 1192.
27 H. Zhou and S. F. Bent, *ACS Appl. Mater. Interfaces*, 2011, **3**, 505.
28 B. H. Lee, B. Yoon, V. R. Anderson and S. M. George, *J. Phys. Chem. C*, 2012, **116**, 3250.
29 Y. S. Min, I. P. Asanov and C. S. Hwang, *Electrochem. Solid-State Lett.*, 2006, **9**, G231.
30 S. K. Kim, G. J. Choi, S. Y. Lee, M. Seo, S. W. Lee, J. H. Han, H. S. Ahn, S. Han and C. S. Hwang, *Adv. Mater.*, 2008, **20**, 1429.
31 M. Halik, H. Klauk, U. Zschieschang, G. Schmid, C. Dehm, M. Schutz, S. Maisch, F. Effenberger, M. Brunnbauer and F. Stellacci, *Nature*, 2004, **431**, 963.
32 H. Klauk, U. Zschieschang, J. Pflaum and M. Halik, *Nature*, 2007, **445**, 745.
33 A. A. Virkar, S. Mannsfeld, Z. Bao and N. Stingelin, *Adv. Mater.*, 2010, **22**, 3857.
34 B. H. Lee, K. H. Lee, S. Im and M. M. Sung, *J. Nanosci. Nanotechnol.*, 2009, **9**, 6962.
35 Y. Park, K. S. Han, B. H. Lee, S. Cho, K. H. Lee, S. Im and M. M. Sung, *Org. Electron.*, 2011, **12**, 348.
36 M. E. Thomas and W. J. Tropf, in *Handbook of Optical Constants of Solids*, ed. E. D. Palik, Academic Press, San Diego, CA, 1998, p. 653.
37 G. E. Jellison, Jr and F. A. Modine, *Appl. Phys. Lett.*, 1996, **69**, 371.
38 B. E. Deal and A. S. Grove, *J. Appl. Phys.*, 1965, **36**, 3770.
39 G. Beamson and D. Briggs, *High Resolution XPS of Organic Polymers: The Scienta ESCA 300 Database*, John Wiley and Sons, Chichester, UK, 1992.
40 D. Briggs, *Surface Analysis of Polymers by XPS and Static SIMS*, Cambridge University Press, Cambridge, UK, 1998.
41 C. H. Schmitz, M. Schmid, S. Gartner, H. P. Steinruck, J. M. Gottfried and M. Sokolowski, *J. Phys. Chem. C*, 2011, **115**, 18186.
42 P. W. Wang, J. C. Hsu, Y. H. Lin and H. L. Chen, *Appl. Surf. Sci.*, 2010, **256**, 4211.
43 P. W. Wang, J. C. Hsu, Y. H. Lin and H. L. Chen, *Surf. Interface Anal.*, 2011, **43**, 1089.
44 J. B. Kim, D. R. Kwon, K. Chakrabarti, C. Lee, K. Y. Oh and J. H. Lee, *J. Appl. Phys.*, 2002, **92**, 6739.
45 M. D. Groner, J. W. Elam, F. H. Fabreguette and S. M. George, *Thin Solid Films*, 2002, **413**, 186.
46 Y. S. Min, Y. J. Cho and C. S. Hwang, *Chem. Mater.*, 2005, **17**, 626.
47 S. M. Sze, *Physics of Semiconductor Devices*, John Wiley and Sons, New Jersey, 3rd edn, 2007, p. 197.
48 D. K. Schroder, *Semiconductor Material and Device Characterization*, John Wiley and Sons, New Jersey, 3rd edn, 2006, p. 319.
49 D. R. Lide, *CRC Handbook of Chemistry and Physics*, CRC Press, Boca Ranton, Fl, 86th edn, 2004, pp. 12–114.
50 T. Hori, *Gate Dielectrics and MOS ULSIs*, Springer, Berlin, 1997, p. 23.
51 D. H. Lee and H. D. Jeong, *J. Phys. Chem. C*, 2008, **112**, 16984.
52 S. Yoshida, T. Ono and M. Esashi, *Nanotechnology*, 2011, **22**, 335302.
53 P. C. Y. Chen, *IEEE Trans. Electron Devices*, 1977, **ED-24**, 584.
54 K. S. Seol, K. S. Cho, B. K. Kim, J. Y. Choi, K. E. Lee, Y. S. Min, J. B. Park and S. H. Choi, *J. Korean Phys. Soc.*, 2007, **50**, 49.
55 A. J. Hong, E. B. Song, H. S. Yu, M. J. Allen, J. Kim, J. D. Fowler, J. K. Wassei, Y. Park, Y. Wang, J. Zou, R. B. Kaner, B. H. Weiller and K. L. Wang, *ACS Nano*, 2011, **5**, 7812.
56 J. K. Choi, S. Jang, K. J. Kim, H. Sohn and H. D. Jeong, *J. Am. Chem. Soc.*, 2011, **133**, 7764.